Proceedings of the ASME 2010 3rd Joint US-European Fluids Engineering Summer Meeting and 8th International Conference on Nanochannels, Microchannels, and Minichannels
FEDSM-ICNMM2010
August 1-5, 2010, Montreal, Canada

FEDSM-ICNMM2010-31199

COMPUTATIONAL METHODOLOGY FOR INTEGRATED CFD-CSD SIMULATIONS OF FLUID-STRUCTURE INTERACTION PROBLEMS

Jinmo Lee
Department of Mechanical Engineering
Carnegie Mellon University
Pittsburgh, Pennsylvania 15213
Email: jinmol@andrew.cmu.edu

Donghyun You*
Department of Mechanical Engineering
Carnegie Mellon University
Pittsburgh, Pennsylvania 15213
Email: dhyou@cmu.edu

ABSTRACT

A newly developed computational methodology for high-fidelity prediction of fluid and structure dynamics and their unsteady interaction is presented. The present methodology combines an immersed-boundary method, which is capable of simulating flow over non-grid-conforming complex moving bodies and a structural dynamics solver, which is based on a finite-element method and is capable of predicting time-accurate dynamics of deforming solid structures. The pressure and velocity of fluid and geometric information of submerged structures are time-accurately coupled through an integration algorithm. The capability of the present computational fluid dynamics (CFD) - computational structure dynamics (CSD) coupling technique is assessed in a number of validation simulations.

INTRODUCTION

Time accurate prediction of fluid-structure interaction has considerable practical significance since fluid-structure interaction often characterizes the performance, efficiency, vibration, and noise emission of many aero-/hydro-dynamic systems such as helicopter rotor blades, wind/hydro turbine blades, pitching and flapping airfoils and wings, and rotating turbomachinery blades. Fluid-structure interaction often takes place at extreme conditions, *e.g.*, very high speed, temperature, and pressure, and in complex configurations. In such cases, simultaneous experimental measurements of fluid and structure dynamics are very difficult and impractical.

Recent advancement of computing powers and computational modeling and simulation technologies allows predicting complex physical phenomena occurring in fluid-structure interactions. A major difficulty in simulations of unsteady fluid-structure interaction phenomena is to design a computational mesh, which can adequately resolve deforming structures. A body-conforming time-varying mesh has often been utilized in finite-element-based methods. Although this approach is capable of capturing the geometric deformation accurately, the method is often limited to the cases with mild structural deformation, which can be resolved with reasonable mesh deformation. Furthermore, for high Reynolds number simulations, finite-element methods, especially high-order accurate, tend to be unstable and therefore, necessitate numerical stabilization. For example, Dettmer and Perić [1] employed a finite-element method utilizing a streamline-upwind and pressure-stabilizing Petrov-Galerkin (SUPG/PSPG) algorithm for a simulation of flow-induced vibration of a flexible beam.

In recent years, finite-difference and finite-volume methods utilizing an immersed boundary method [2] have received special attention for simulation of fluid-structure interaction problems. Compared to body-conforming grid methods, an immersed-boundary method utilizes a simple Cartesian grid and imposes necessary boundary conditions on non-grid conforming boundaries of structures. Although immersed boundary methods can handle complex moving geometries, the methods have been mostly applied to fluid-structure interaction problems where the

*Corresponding author. Tel.: +1 412 268 6808; fax: +1 412 268 3348

deformation and motions of solid structures are prescribed.

In the present study, we develop a computational methodology for high-fidelity prediction of both fluid and structure dynamics and their unsteady interaction. The present methodology combines an immersed-boundary method, which is capable of simulating flow over non-grid-conforming complex moving bodies and a structural dynamics solver, which is based on a finite-element method and is capable of predicting time-accurate linear and non-linear dynamics of solid structures. In contrast to the conventional immersed boundary method, where the structural dynamics is not predicted but prescribed, in the present method, the structural dynamics is directly computed using a finite-element-based method. The pressure and velocity of fluid and geometric information of submerged structures are time-accurately coupled through an integration algorithm.

COMPUTATIONAL METHODOLOGY

A. Numerical method for fluid flow

The numerical method is based on a Cartesian-coordinate Navier-Stokes solver originally developed by You *et al.* [3], with significant enhancements to treat complex moving geometries. The incompressible Navier-Stokes equations are as follows:

$$\frac{\partial u_i}{\partial t} + \frac{\partial}{\partial x_j} u_i u_j = -\frac{\partial p}{\partial x_i} + \frac{1}{Re}\frac{\partial}{\partial x_j}\frac{\partial u_i}{\partial x_j}, \tag{1}$$

$$\frac{\partial u_i}{\partial x_i} = 0, \tag{2}$$

where $i, j = 1, 2$, and 3. u_i is the velocity component in the i-direction. All of the coordinate variables, velocity components, and pressure are nondimensionalized by a length-scale L, the inflow freestream velocity U_∞, and $\rho_f U_\infty^2$, respectively. The time is normalized by L/U_∞. The Reynolds number is defined as $Re = \frac{U_\infty L}{\nu}$, where ν is the kinematic viscosity of the fluid. The pressure and velocity components are arranged and discretized on a collocated grid as shown in Fig. 1. A fractional step method is used for time integration. For the convective terms, a second order Adams-Bashforth scheme is employed, while a second-order Crank-Nicolson scheme is used for the diffusion terms. The discretized momentum equations can be written as

$$\frac{u_i^* - u_i^n}{\Delta t} + \frac{1}{2}[3N_i^n - N_i^{n-1}] = -\frac{\delta p^n}{\delta x_i} + \frac{1}{2Re}(D_i^* + D_i^n), \tag{3}$$

where $N_i = \frac{\delta(U_j u_i)}{\delta x_j}$ and $D_i = \frac{\delta}{\delta x_j}(\frac{\delta u_j}{\delta x_i})$ represent the convective and diffusive terms, respectively, while $\frac{\delta}{\delta x}$ denotes a spatial discretization operator. The cell-center velocity u_i^* is computed

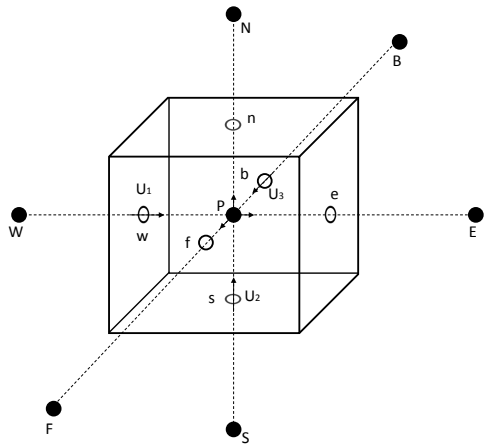

Figure 1. Illustration of a collocated-grid arrangement of primitive variables.

using a Line SOR scheme with a Gauss-Siedel method as a smoother, while the face-center velocity U^* is computed as follows:

$$\begin{aligned}
\tilde{u_i} &= u_i^* + \Delta t(\frac{\delta p^n}{\delta x_i})_{cc},\\
\widetilde{U_1} &= \gamma_w \tilde{u}_{1P} + (1-\gamma_w)\tilde{u}_{1W},\\
\widetilde{U_2} &= \gamma_s \tilde{u}_{2P} + (1-\gamma_s)\tilde{u}_{2S},\\
\widetilde{U_1} &= \gamma_b \tilde{u}_{3P} + (1-\gamma_b)\tilde{u}_{3B},\\
U_i^* &= \widetilde{U_i} - \Delta(\frac{\delta p^n}{\delta x_i})_{fc},
\end{aligned} \tag{4}$$

where γ_w, γ_s, and γ_b are the linear interpolation weights for the face velocity components in the west, south, and back directions, respectively. Subscrips of cc and fc represent the cell and face centers, respectively. The velocity u_i^{n+1} is computed by a pressure-correction as follows:

$$\frac{u_i^{n+1} - u_i^*}{\Delta t} = -\frac{\delta p'}{\delta x_i}, \tag{5}$$

where $p' = p^{n+1} - p^n$.

The equation (5) and the divergence free condition for u_i^{n+1} result in a Poisson equation as follows:

$$\frac{\delta}{\delta x_i}(\frac{\delta p'}{\delta x_i}) = \frac{1}{\Delta t}\frac{\delta U_i^*}{\delta x_i}. \tag{6}$$

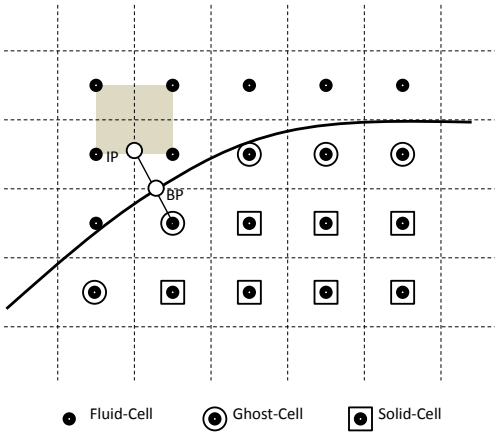

Figure 2. Definitions of the fluid, solid, and ghost cells in the present immersed boundary method.

The Poisson equation is solved using a multigrid method. The velocity and pressure components are updated as

$$\begin{aligned} p^{n+1} &= p^n + p^{'}, \\ u_i^{n+1} &= u_i^* - \Delta t(\frac{\delta p^{'}}{\delta x_i})_{cc}, \\ U_i^{n+1} &= U_i^* - \Delta t(\frac{\delta p^{'}}{\delta x_i})_{fc}. \end{aligned} \tag{7}$$

B. Immersed boundary method

The present immersed boundary method is based on a ghost-cell method proposed by Mittal *et al.* [4], and allows to effectively handle complex moving and stationary bodies. Complex geometries are represented with triangular surface elements. The inside and outside of a submerged object are identified by a dot product of the surface element normal vector and the position vector which extends to the node from the closest surface element. If the dot product has a positive (negative) value, the node is identified as the outside (inside) of a submerged body.

The cells identified as the outside and inside of a submerged body correspond to fluid and solid, respectively, while the cells located at the interface between the outside and inside cells are defined as ghost cells as illustrated in Fig. 2.

The velocity and pressure are not assigned to the solid cells, while the variables are assigned to the ghost cells to impose the necessary boundary condition on the immersed boundary. The flow field variables on ghost cells are interpolated using the values at the associated image point, and boundary intercepts. A flow variable ϕ at the image point is interpolated using surrounding eight nodes as follows:

$$\begin{aligned} \phi(x_1,x_2,x_3) = C_1x_1x_2x_3 + C_2x_1x_2 + C_3x_2x_3 + C_4x_1x_3 \\ + C_5x_1 + C_6x_2 + C_7x_3 + C_8. \end{aligned} \tag{8}$$

The eight unknown coefficients C_i can be determined by solving the following algebraic equation:

$$\{C\} = [V]^{-1}\{\phi\}, \tag{9}$$

where

$$\{C\}^T = \{C_1, C_2, ..., C_8\}, \tag{10}$$

$$\{\phi\}^T = \{\phi_1, \phi_2, ..., \phi_8\}, \tag{11}$$

$$[V] = \begin{bmatrix} x_1x_2x_3|_1 & x_1x_2|_1 & x_1x_3|_1 & x_2x_3|_1 & x_1|_1 & x_2|_1 & x_3|_1 & 1 \\ x_1x_2x_3|_2 & x_1x_2|_2 & x_1x_3|_2 & x_2x_3|_2 & x_1|_2 & x_2|_2 & x_3|_2 & 1 \\ \vdots & \vdots & \vdots & \vdots & & & & \\ x_1x_2x_3|_8 & x_1x_2|_8 & x_1x_3|_8 & x_2x_3|_8 & x_1|_8 & x_2|_8 & x_3|_8 & 1 \end{bmatrix}. \tag{12}$$

A flow variable ϕ at an image point can be expressed using the computed C_i as follows:

$$\phi_{IP} = \sum_{i=1}^{8} \beta_i\phi_i + T.E., \tag{13}$$

$$\begin{aligned} \beta^T = \\ \{x_1x_2x_3|_{IP}\ x_1x_2|_{IP}\ x_1x_3|_{IP}\ x_2x_3|_{IP}\ x_1|_{IP}\ x_2|_{IP}\ x_3|_{IP}\ 1\}[V]^{-1}\{\phi\}, \end{aligned} \tag{14}$$

where $T.E.$ denote a leading-order truncation error.

A flow variable at a ghost cell, ϕ_{GC}, is now calculated using the values at the image point and boundary intercept with a linear interpolation technique:

$$\begin{aligned} \phi_{BI} &= \frac{1}{2}(\phi_{IP} + \phi_{GC}) + O(\Delta l^2) \\ &= \frac{1}{2}(\sum_{i=1}^{8} \beta_i\phi_i + \phi_{GC}) + O(\Delta^2) + O(\Delta l^2), \end{aligned} \tag{15}$$

where Δl is the distance between a ghost cell and an image point. The equation (15) can be recast into an implicit form:

$$\phi_{GC} = 2\phi_{BI} - \sum_{i=1}^{8} \beta_i\phi_i. \tag{16}$$

A Neumann boundary condition can be also imposed on a boundary interface as follows:

$$(\frac{\delta\phi}{\delta n})_{BI} = \frac{\phi_I P - \phi_G C}{\Delta l} + O(\delta l^2)$$
$$= \frac{1}{\Delta l}(\sum_{i=1}^{8}\beta_i\phi_i - \phi_G C) + O(\Delta^2/\Delta l^2) + O(\Delta l^2), \quad (17)$$
$$\phi_{GC} = \sum_{i=1}^{8}\beta_i\phi_i - \Delta l(\frac{\delta\phi}{\delta n})_{BI}. \quad (18)$$

The governing equations are solved for the flow variables at the fluid and ghost cells, while the required boundary condition on the immersed boundary is satisfied.

C. Numerical method for solid dynamics

A dynamic motion of an immersed solid structure is computed using an implicit-explicit time integration of the discrete equation of motion as proposed by Miranda, Ferencz, and Hughes [5]:

$$\mathbf{M}\mathbf{a}_{n+1} + (1+\alpha)\mathbf{C}\mathbf{v}_{n+1} - \alpha\mathbf{C}\mathbf{v}_{\mathbf{n}} + (1+\alpha)\mathbf{K}\mathbf{d}_{n+1} - \alpha\mathbf{K}\mathbf{d}_n$$
$$= \mathbf{F}^{ext}_{n+1+\alpha} \stackrel{def}{=} (1+\alpha)\mathbf{F}^{ext}_{n+1} - \alpha\mathbf{F}^{ext}_{n}, \quad (19)$$

where $\mathbf{M}$ is the mass matrix, $\mathbf{C}$ is the damping matrix, $\mathbf{K}$ is the stiffness matrix, and $\mathbf{F}^{ext} = \mathbf{f}^{ext}(t)$ is an external force vector. $\mathbf{d}_n$, $\mathbf{v}_n$, and $\mathbf{a}_n$ are approximated vectors of the nodal displacements, velocities, and accelerations at the time step of $t_n = n\Delta t$. The displacements, and velocity vectors are calculated using the difference formulae of Newmark [6]:

$$\mathbf{d}_{n+1} = \mathbf{d}_n + \Delta t\mathbf{v}_n + \frac{1}{2}\Delta t^2[(1-2\beta_d)\mathbf{a}_n + 2\beta_d\mathbf{a}_{n+1}],$$
$$\mathbf{v}_{n+1} = \mathbf{v}_n + \Delta t[(1-\gamma_d)\mathbf{a}_n + \gamma_d\mathbf{a}_{n+1}]. \quad (20)$$

The accuracy and stability of the present method rely on the choice of α, β_d, and γ_d. In the present study $\beta_d = \frac{1}{4}(1-\alpha)^2$, and $\gamma_d = \frac{1}{2} - \alpha$, and the choice makes this scheme be second-order accurate as well as unconditionally stable in the interval of $\alpha \in [-\frac{1}{3}, 0]$. The time-discrete equation is solved using a predictor-corrector algorithm as follows:
Predictor step:

$$\tilde{\mathbf{d}}_{n+1} = \mathbf{d}_n + \Delta t\mathbf{v}_n + \frac{1}{2}(1-2\beta_d)\Delta t^2\mathbf{a}_n,$$
$$\tilde{\mathbf{v}}_{n+1} = \mathbf{v}_n + (1-\gamma_d)\Delta t\mathbf{a}_n. \quad (21)$$

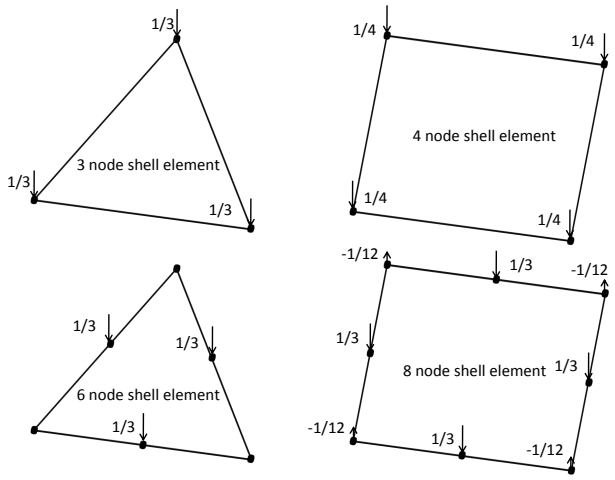

Figure 3. Nodal distribution of a unit load.

Solution of the equation of motion:

$$\mathbf{M}\mathbf{a}_{n+1} + (1+\alpha)\mathbf{C}\tilde{\mathbf{v}}_{n+1} - \alpha\mathbf{C}\mathbf{v}_n + (1+\alpha)\mathbf{K}\tilde{\mathbf{d}}_{n+1} - \alpha\mathbf{K}\mathbf{d}_n$$
$$= \mathbf{F}^{ext}_{n+1+\alpha}. \quad (22)$$

Corrector step:

$$\mathbf{d}_{n+1} = \tilde{\mathbf{d}}_{n+1} + \beta_d\Delta t^2\mathbf{a}_{n+1},$$
$$\mathbf{v}_{n+1} = \tilde{\mathbf{v}}_{n+1} + \gamma_d\Delta t\mathbf{a}_{n+1}. \quad (23)$$

D. CFD-CSD Integration

Integration of the computational fluid dynamics (CFD) and computational structural dynamics (CSD) codes is realized through an exchange of the geometric and force information during time integration steps. Surface mesh elements on deforming structures, of which dynamic motions are computed by the CSD code, is transferred to the CFD code which is based on an immersed-boundary method. In the present method, rectangular- and triangular-shape elements are used for the CSD code and for an immersed boundary identification routine, respectively. Therefore, the rectangular elements are split to construct triangular-shape surface elements required for the immersed boundary identification routine.

Transformation of surface elements is needed only at the initial step of the simulation. Thereafter, only the change of coordinates of surface elements due to structural deformation is accounted for by the immersed boundary method. Locations of ghost cells and boundary intercepts are identified on the newly deformed surface elements, and necessary interpolation steps are

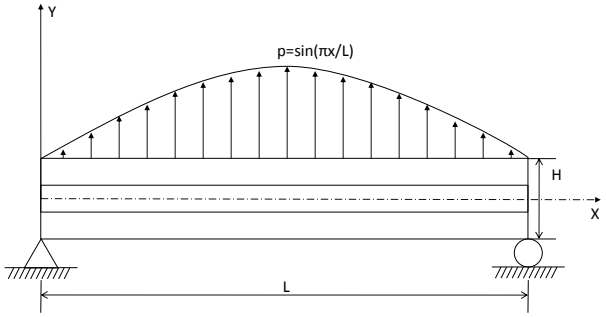

Figure 4. Simply supported 3-ply plate subject to cylindrical bending, where H=3 and L=12.

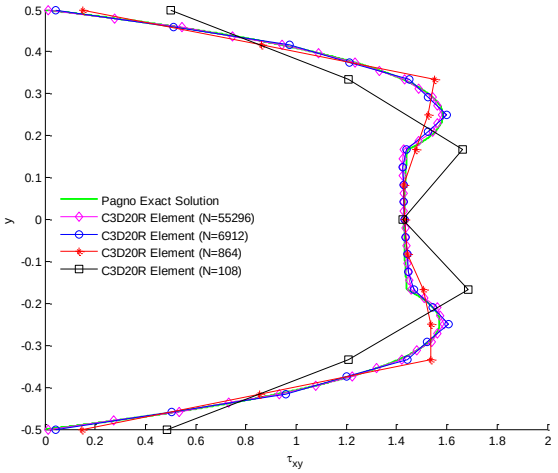

Figure 5. Shear stress distribution along y-axis at the middle of the plate.

followed to impose boundary conditions on the surface of immersed structures. Once the pressure and velocity components are computed in the flow field over immersed structures, normal and tangential forces imposed on the surfaces of the structures are computed. The computed normal and tangential forces are distributed to the nodal points of the surface elements for the CSD analysis as illustrated in Fig. 3. The CSD code solves the discrete equation of motion of a structure under the forces imposed by the fluid flow to find the deformation of the structure. Then, the updated geometric information of the structure transferred to the immersed boundary identification routine to continue the simulation of fluid flow in the next time step.

ASSESSMENT OF THE PROPOSED METHODOLOGY

A. Validation of the CSD code

The predictive capability as well as the computational efficiency of the present CSD code is assessed in simulations of deformation of a simply supported 3-ply plate subject to a cylindrical bending load as shown in Fig. 4. Each layer of the 3-ply plate consists of unidirectional fibrous material with different fiber orientation, $0^\circ - 90^\circ - 0^\circ$. Material properties of this unidirectional fibrous material are $E_1 = 172.4GPa$, $E_2 = 6.90GPa$, $G_{12} = 3.45GPa$, $\nu_{12} = 0.25$, where 1 and 2 denotes longitudinal and transverse directions to the fiber, respectively, E is the Young's modulus, G is the shear modulus, and ν is the Poisson's ratio. In the present simulations, about 100 to 55,000 20-noded continuum solid elements with reduced integration (C3D20R) are employed. Figure. 5 and 6 are the shear stress and normal stress distributions, respectively, at the middle of the plate, and

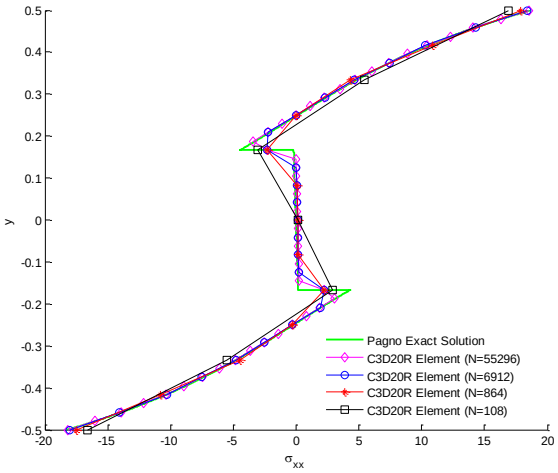

Figure 6. Normal stress distribution along y-axis at the middle of the plate.

in these figures, the present numerical solution are found to converge to an exact solution of Pagno [7] with increasing number of elements. The present numerical method shows second-order spatial convergence.

B. Validation of the CFD code

Vortex shedding behind a circular cylinder The accuracy and effectiveness of the present immersed-boundary method is evaluated in the simulation of flow over a stationary circular cylinder. The computational domain size is $40d \times 40d$ and the number of grid points is 451×451, where d is the cylin-

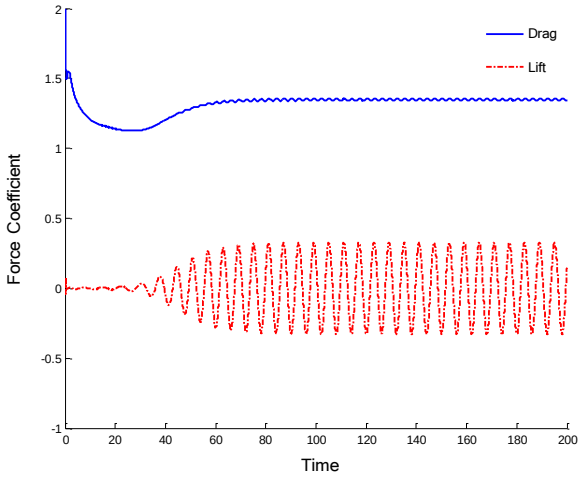

Figure 7. Laminar vortex shedding simulation drag and lift force history.

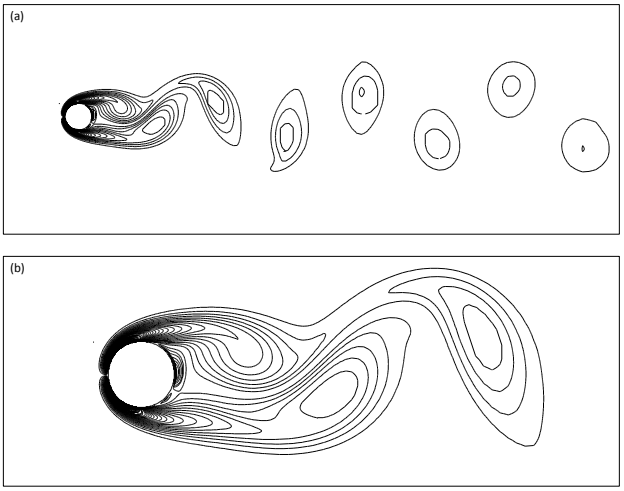

Figure 8. (a) is contour of the instantaneous spanwise vorticity magnitude over a stationary circular cylinder at Re=100, and (b) is the enlarged image of (a) around the cylinder.

der diameter. Time histories of the drag and lift coefficients are shown in Fig. 7. The grid lines are clustered around the cylinder and the minimum grid spacing is $0.01d$. The time-step size is fixed to 0.005 and it corresponds to the CFL number of 0.77 - 1.11. As summarized in Table 1, the drag and lift coefficients and the Strouhal number predicted by the present method are found to agree well the results obtained using a curvilinear body-fitted-mesh method (You *et al.* [8]). The advantage of using a kinetic-energy conserving, non-dissipative numerical scheme is clearly identified in Fig. 8(a), which shows well-organized vortices far

Table 1. Drag and lift coefficients, and Strouhal number at Re=100.

	C_L	C_D	St
Present	0.232	1.348	0.167
You *et al.* [8]	0.229	1.306	0.166

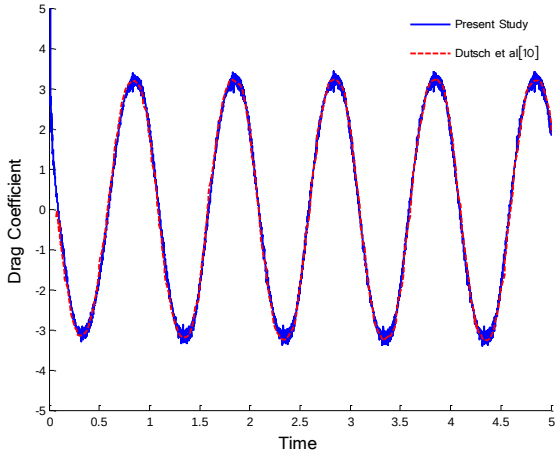

Figure 9. Time history of the drag force on an oscillating cylinder at Re=100.

away from the cylinder. As shown in Fig. 8(b), smooth contour lines around the cylinder indicate that the present immersed boundary method accurately resolves a boundary layer over a non-grid-conforming cylinder surface.

Flow over an oscillatory cylinder Flow over a periodically oscillating cylinder, which was previously studied by Dütsch *et al.* [9], is simulated to assess the predictive capability of the presented immersed boundary method for a moving immersed structure. A periodic motion of a circular cylinder is prescribed with the Keulegan-Carpenter number of 5. The Reynolds number is 100, based on the cylinder diameter and the maximum velocity of the oscillation. The domain size is $50d \times 50d$ and the grid size is 353×193. The grid lines are clustered around the cylinder with the minimum spacing of $0.01d$. The time-step size is fixed to 0.01, which corresponds to the CFL number of 0.55 - 0.75. As shown in Fig. 9, the drag coefficient predicted by the present method is found to agree well with the result of Dütsch *et al.* [9], which was computed using a body-fitted grid approach. Figure. 10 shows the instantaneous vorticity and pressure contours around an oscillating cylinder at the phase of 0° and 288°,

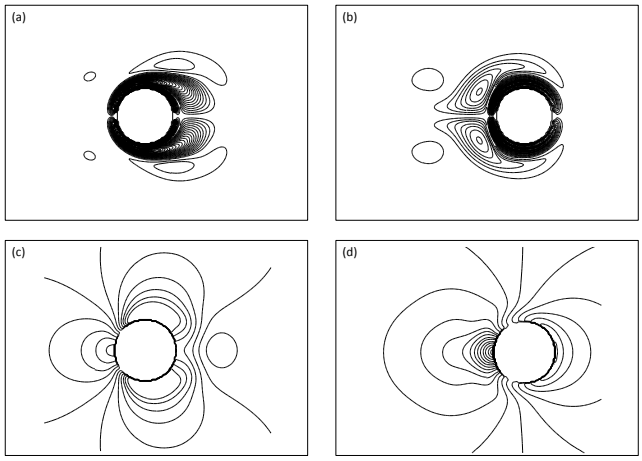

Figure 10. Contours of the instantaneous spanwise vorticity ((a) and (b)) and pressure ((c) and (d)) over an oscillatory cylinder. (a) and (c) are at the phase angle of 0°, and (b) and (d) are at the phase angle of 288°.

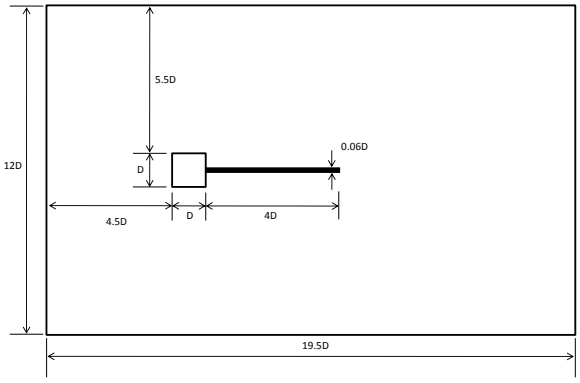

Figure 11. Computational configuration for a simulation of flow over a square cylinder with a flexible splitter plate

and these phenomena are found to qualitatively agree well with the result of Dütsch *et al.* [9].

C. Integrated CFD-CSD simulation

Flow-induced vibration of a flexible beam The capability of the present CFD-CSD integration technology is being evaluated in a simulation of flow over a square cylinder with a flexible splitter plate attached to the rear stagnation point. The configuration has been extensively studied by other previous researchers (Hübner [10], Steindorf [11], Dettmer and Peric [1]).

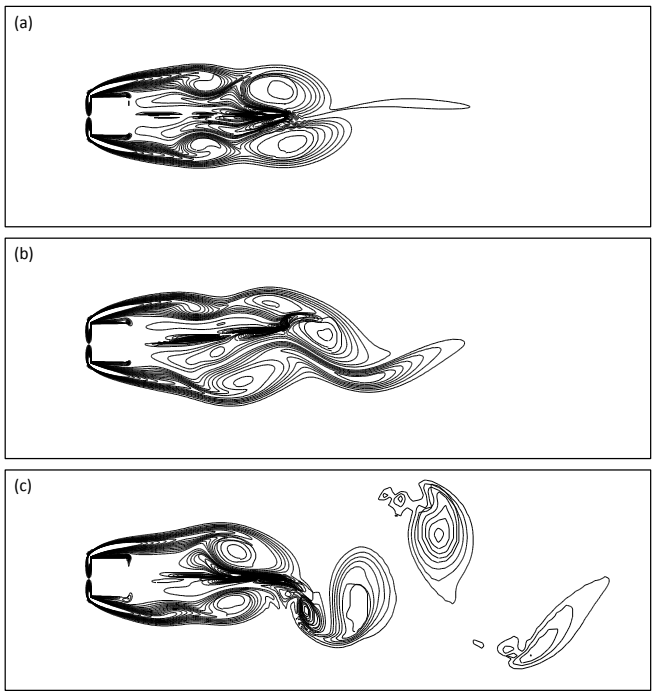

Figure 12. Contours of the instantaneous spanwise vorticity. (a) $t = 0.39$, (b) $t = 0.49$, and (c) $t = 0.58$.

The flow configuration is schematically shown in Fig. 11. The fluid and structure properties are $\mu^f = 1.82 \times 10^{-4}$, $\rho^f = 1.18 \times 10^{-3}$, $\mu^s = 9.2593 \times 10^5$, $\rho^f = 0.1 \times 10^{-3}$, $E = 2.5 \times 10^6$, and $\nu = 0.35$, where superscripts f and s denote fluid and structure, E is the Young's modulus, and ν is the Poisson's ratio. The Reynolds number is $Re = \rho^f D u_\infty / \mu^f = 333$, where D and U_∞ are the height of the square cylinder and the freestream velocity, respectively. In CFD analysis, the domain size is $12D \times 19.5D$, and the grid size is 309×301. The grid lines of CFD analysis are clustered around the square cylinder with the minimum spacing of $0.01D$. The time step size of CFD analysis, which is normalized by square cylinder diameter and freestream velocity, is 0.002. For the CSD analysis, 76 C3D20R elements are used, and plane strain condition is assumed.

As shown in Fig. 12, flow over a square cylinder produces vortex shedding, which causes alternating pressure and shear stress distributions over the flexible splitter plate. As a result, the flexible splitter plate vibrates periodically with a certain magnitude of displacement. The displacement of the splitter plate tip is presented in Fig. 13.

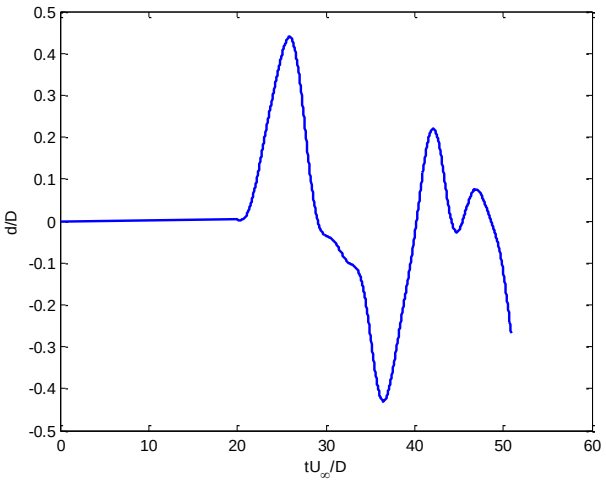

Figure 13. Flow induced vibration of a flexible splitter, where d/D is the vertical displacement of a flexible splitter tip and tU_∞/D is time.

SUMMARY

A computational methodology for high-fidelity time-accurate prediction of fluid and structure dynamics and their unsteady interaction has been developed. The present methodology combines an immersed-boundary method, which is capable of simulating flow over non-grid-conforming complex moving bodies and a structural dynamics solver, which is based on a finite-element method and is capable of predicting time-accurate dynamics of solid structures. The pressure and velocity of fluid and geometric information of submerged structures are time-accurately coupled through an integration algorithm. The standalone predictive capabilities of the CFD and CSD codes have been extensively validated in a number of simulations.

The capability of the present CFD-CSD coupling methodology is being assessed in the simulation of flow over a square cylinder with a flexible splitter plate.

REFERENCES

[1] W. Dettmer, D. Perić, 2006. A computational framework for fluid-structure interaction: Finite element formulation and applications, *Comput. Methods Appl. Mech. Engrg.*, Vol. 195, pp. 5754-5779.

[2] R. Mittal, G. Iaccarino, 2005. Immersed boundary method, *Annu. Rev. Fluid Mech.*, Vol. 37, pp. 239-261.

[3] D. You, R. Mittal, M. Wang, P. Moin, 2004. Computational methodology for large-eddy simulation of tip-clearance flows, *AIAA Journal*, Vol. 42, pp. 271-279.

[4] R. Mittal, H. Dong, M. Bozkurttas, F. M. Najjar, A. Vargas, A. von Loebbecke, 2008. A versatile sharp interface immersed boundary method for incompressible flows with complex boundaries, *Journal of Computational Physics*, Vol. 227, pp. 4825-4852.

[5] I. Miranda, R. M. Ferencz, T. J. R. Hughes, 1989. An improved implicit-explicit time integration method for structural dynamics, *Earthquake Engineering and Structural Dynamics*, Vol. 18, pp. 643-653.

[6] N. M. Newmark, 1959. A method of computation for structural dynamics, *Journal of Engineering Mechanics*, Vol. 85, pp. 67-94.

[7] N. J. Pagno, 1969. Exact solutions for composite laminates in cylindrical bending, *Journal of Composite Materials*, Vol. 3, pp. 398-411.

[8] D. You, H. Choi, M.-R. Choi, S.-H. Kang, 1998. Control of flow-induced noise behind a circular cylinder using splitter plates, *AIAA Journal*, Vol. 36, pp. 1961-1967.

[9] H. Dütsch, F. Durst, S. Becker, H. Lienhart, 1998. Low-Reynolds-number flow around an oscillating circular cylinder at low Keulegan-Carpenter numbers, *Journal of Fluid Mechanics*, Vol. 360, pp. 249-271.

[10] B. Hübner, E. Walhorn, 2004. A monolithic approach to fluid-structure interaction using space-time finite elements, *Comput. Methods Appl. Mech. Engrg.*, Vol. 193, pp. 2087-2104.

[11] J. Steindorf, 2003. Partitionierte verfahren für probleme der fluid-struktur wechselwirkung, Ph.D. thesis, Technische Universität Braunschweig, Mechanik-Zentrum.